2012 IEEE International Conference on Robotics and Automation
RiverCentre, Saint Paul, Minnesota, USA
May 14-18, 2012

Motion planning for Multiple Millimeter-scale Magnetic Capsules in a Fluid Environment

Panagiotis Vartholomeos, *Member, IEEE*, M.Reza Akhavan-Sharif
and Pierre E. Dupont, *Fellow, IEEE*

Abstract— **There are many examples of minimally invasive surgery in which tethered robots are incapable of accurately reaching target locations deep inside the body either because they are too large and result in tissue damage or because the tortuosity of the path leads to loss of tip control. In these situations, small untethered magnetically-powered robots may hold the potential to act as delivery vehicles for therapeutic agents. While MRI scanners provide a means to power, control and image such robots as they move throughout the body, a substantial challenge arises if the clinical application requires more than one such robot. The resulting system is underactuated and thus its controllability is in question. This paper presents a simple motion planning algorithm for two magnetic capsules and demonstrates through simulation and experiment that nonlinear fluid damping can be exploited to independently control the positions of the capsules.**

I. Introduction

FLUID filled pathways within the body provide natural highways for groups of small robots to reach tissue targets with minimal damage. The ventricles, for example, provide access throughout the brain and can be reached via the spinal canal. Robots injected into the spine could be directed to any desired targets within the ventricles. If properly equipped, they could provide highly targeted delivery of drugs within the brain. Alternately, they could distribute a network of sensors that could be used to monitor for abnormal pressure distributions. Depending on the application, the robots could be designed to be biodegradable, e.g., for drug delivery, or could simply be controlled to swim back down the spine for retrieval. In contrast to the circulatory system, the relative uniformity of cerebrospinal fluid spaces and the low flow rate of cerebrospinal fluid make the brain a hospitable environment for such robots.

We are not the first to propose such magnetically controlled robots. Excellent work has been performed by a number of groups on this topic. For example, micrometer scale swimming robots have been demonstrated in [1-5] and proposed for use in a variety of medical applications including drug delivery within the eye [6] and targeted chemotherapeutic delivery through the vasculature [7].

Besides swimming, researchers have also considered magnetically powered robots moving on a planar surface [8], [9]. Most of the research to date has been focused on optimizing the design and motion control of individual robots. Also, much of the work has been conducted using custom magnetic coils while only a few investigators have employed clinical MRI scanners [1,4,5]. This choice has a substantial effect on the control methods available.

Furthermore, past work has focused on micron-scale robots that operate at low Reynolds numbers and so experience Stokes flow. In contrast, only a few researchers have considered motion control at the millimeter scale. In particular, MRI control of a 2.5 mm ball bearing in the carotid artery of a pig was demonstrated in [10].

Millimeter-scale magnetic robots offer advantages for some clinical applications since they can produce larger magnetic forces and carry larger payloads. They operate at higher Reynolds numbers (1-1000), however, and so must be modeled using quadratic damping at high speeds.

The topic that has received the least attention in the literature is that of controlling groups of magnetic robots. Group control is an important problem in medical applications since the size of an individual robot limits its payload in drug delivery applications. Furthermore, it may be necessary to deliver drugs over a sustained period of time to multiple locations – which could be easily accomplished if multiple robots could be directed to the individual sites.

Group robot control is difficult because the same magnetic field is applied to all of the robots. For such underactuated systems, independent control can be achieved by exploiting nonlinearities in the system dynamics. This approach has been recently demonstrated for magnetic microrobots on a planar surface in a fluid using custom coils [8]. By designing the robots to maximize the difference in their stick-slip properties on the planar surface, it is possible to design a motion planner to achieve independent control their position on the plane [8].

The contribution of this paper is to provide a motion planner for millimeter-scale robots swimming freely in a fluid and powered by an MRI scanner. We show that, unlike the case of very low Reynolds numbers, the combination of inertial dynamics and drag forces provided by quadratic fluid damping at this size scale enables independent control of robots that possess differences in either drag cross section or magnetic material.

The paper is arranged as follows. The next section describes the capsule robots and provides their dynamic

This work was supported by the Wyss Institute for Biologically Inspired Engineering and by the National Institutes of Health under grant R01HL073647.

P. Vartholomeos and P. Dupont are with Cardiovascular Surgery, Children's Hospital Boston, Harvard Medical School, Boston MA, 02115, USA. {panagiotis.vartholomeos, pierre.dupont}@childrens.harvard.edu.

M.Reza Akhavan-Sharif is with the Beth Israel Deaconess Medical Center, Boston MA, 02215, USA. rakhavan@bidmc.harvard.edu.

model. The third section provides a motion planning method based on the differentiated responses of the robots to pulse sequences of different durations. The properties of the motion planner are illustrated through simulation in the subsequent section and confirmed through experiment in Section V. Conclusions appear in the final section.

II. Dynamics of Two Magnetic Particles

Each capsule consists of a smooth external hollow sphere that encapsulates an internal smaller ferrous sphere (Figure 1a). The two capsules are immersed into a tank with fluid and are placed within the magnetic field $\mathbf{B}_0$ of an MRI scanner. Buoyancy and gravitational forces counteract each other by design and therefore they will be neglected in the following analysis.

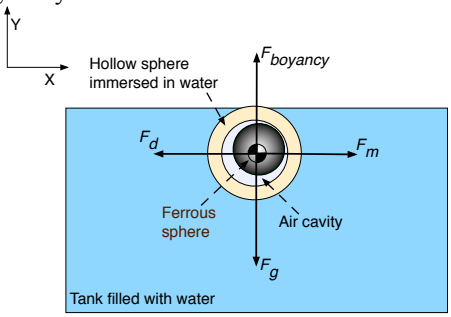

Figure 1. Free body diagram of capsule immersed in water.

A. Drag force

The fluid is assumed to have zero flow. This is a reasonable assumption since in most human cavities the fluid flow is either zero or is very slow. The viscosity and the density of the fluid are similar to those of water. The fluid remains in a laminar region during the capsule's motion and the drag force is given by:

$$F_d = \frac{1}{2}\rho C_d A \mathbf{u}^2 \tag{1}$$

where ρ is the density of the fluid, A is the frontal area of the sphere and $\mathbf{u}$ is the capsule's velocity. The parameter C_d is the drag coefficient and is given by [11]:

$$C_d = \frac{24}{\mathrm{Re}} + \frac{6}{1+\sqrt{\mathrm{Re}}} + 0.4 \tag{2a}$$

and

$$\mathrm{Re} = ||\mathbf{u}||\rho d / \eta \tag{2b}$$

is the capsule's Reynolds number, where d is the capsule's diameter and η is its dynamic viscosity. The use of Eq. (2) can be justified because the Reynolds number is expected to be larger than 1000 [11].

B. Magnetic force

The magnetization across the volume of the ferrous sphere can be approximated as a lumped effect at the center of mass (CM) of the body [12]. Consequently, the magnetized body is approximated by a magnetic dipole placed at its CM. Inside the MRI its magnetization becomes saturated due to the strong magnetic field $\mathbf{B}$ (>1.5T) and is denoted by $\mathbf{M}_s$. The magnetic force $\mathbf{F}_m$ acting on the ferrous sphere of volume V is given by [13]:

$$\mathbf{F}_m = V(\mathbf{M}_s \cdot \nabla)\mathbf{B} = VM_{sz}\left[\ \frac{\partial B_x}{\partial z}\quad \frac{\partial B_y}{\partial z}\quad \frac{\partial B_z}{\partial z}\ \right] \tag{3}$$

where $\partial B/\partial z, \{i = x, y, z\}$ are the three independent magnetic gradients of the MRI, and it has been reasonably assumed that $M_{sx}, M_{sy} << M_{sz}$ due to the very strong $\mathbf{B}_0$ field of the MRI [13].

The present analysis assumes that the magnetic interaction between two or more capsules is negligible. This is a reasonable assumption because using the dipole-dipole magnetic interaction formulas ([14]) it can be shown that the magnetic interaction force decays as a function of the separation distance to the power of four and becomes negligible compared to MRI gradient forces after approximately a separation distance equal to 20 diameters. For example if the ferrous sphere diameter is 500 μm then a 10mm separation distance is sufficient to consider the magnetic interaction negligible with respect to the MRI gradient forces.

C. Equations of motion

The equations of motion for the case of two particles are given by:

$$\begin{aligned} m_1\mathbf{a}_1 &= \mathbf{F}_{d1} + \mathbf{F}_{m1} \\ m_2\mathbf{a}_2 &= \mathbf{F}_{d2} + \mathbf{F}_{m2} \end{aligned} \tag{4}$$

where $\mathbf{F}_{di}$, $\mathbf{F}_{mi}$, $i = \{1,2\}$ are the drag force and the magnetic force correspondingly, and $\mathbf{a} = [\ \ddot{x}\quad \ddot{y}\quad \ddot{z}\ ]$. The x component of Eq. (4) is given by:

$$\begin{aligned} \ddot{x}_1 &= -\frac{b_1}{m_1}\dot{x}_1^2 sign(\dot{y}) + \frac{g_1}{m_1}v \\ \ddot{x}_2 &= -\frac{b_2}{m_2}\dot{x}_1^2 sign(\dot{y}) + \frac{g_2}{m_2}v \end{aligned} \tag{5}$$

where $g_i = V_i M_{szi} / m_i$, $b_i = \pi\rho C_{di} A_i / (2m_i)$, $v = \partial B_z / \partial x$, and $i = \{1,2\}$. Similar scalar expressions hold for the y and z components.

III. Motion Control

A. Controllability

The system of (4) has three orthogonal inputs that independently determine the control of motion in each of the three axes. Therefore, it is sufficient to consider the controllability analysis performed for particle motion along a single axis using (5). The results can be directly generalized

to 3D motion.

Equation (5) is a second order nonlinear system with drift. When more than one particle is present then the system has only one control input (the magnetic gradient) and more than one degrees of freedom, hence the system is underactuated. The linearized state equations are not controllable. Furthermore, the sufficiency conditions for small time local controllability (STLC) given by Sussmann [15] are not satisfied. Hence, nothing can be inferred on the controllability properties of the system.

Intuition suggests, however, that the nonlinear damping in combination with inertial transients may enable motion differentiation for sufficiently different capsule parameter values. To investigate this possibility, control inputs to specifically excite the system's transient response were considered resulting in the motion planning algorithm described below

B. Motion planning algorithm

Consider the case when two particles described by (5) and possessing different parameter values are driven by a sequence of pulses that have width Δt_1, Δt_2 (Figure 2). During each pulse, the particles accelerate. Depending on the width of the pulse the particles may reach terminal speed or they may remain in the transient phase. Each pulse is always followed by a zero input of Δt_{off} duration that is sufficiently long for the capsules to coast to rest.

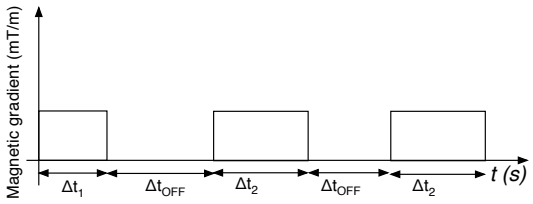

Figure 2. Sequence of control pulses.

Pulses of sufficiently long duration drive the particles into steady-state motion, where the displacement of one particle is proportional to the displacement of the other particle. This equality constraint on particles' position reduces the configuration space of two particles to a single dimension, i.e. the particles cannot be driven independently to goal positions. Sufficiently short pulses, however, drive the particles in the transient phase and produce variations in relative displacement depending on their duration. This is borne out in Figure 3 and Figure 4 that plot displacements and the ratio of displacements versus pulse width.

It can be observed that while the ratio of displacements does approach a constant value of about 1.3 for pulses greater than 0.1 sec, its value is variable for shorter duration pulses. Thus, to independently drive the two capsules to desired locations, it is only necessary to pick two pulse widths that provide sufficiently different ratios of displacement. The individual displacements, written as $x_i(\Delta t_i), \{i = 1,2\}$, can be arranged in a matrix form called the control matrix **R** to provide a linear equation relating the desired particle final displacements, x_1^f and x_2^f to the numbers n_1 and n_2 of pulses of duration Δt_1 and Δt_2, respectively.

$$\begin{bmatrix} x_1^f \\ x_2^f \end{bmatrix} = \begin{bmatrix} x_1(\Delta t_1) & x_1(\Delta t_2) \\ x_2(\Delta t_1) & x_2(\Delta t_2) \end{bmatrix} \begin{bmatrix} n_1 \\ n_2 \end{bmatrix} = \mathbf{Rn} \quad (6)$$

The following two figures depict: (1) the step length of the particles as a function of the pulse width Δt and (2) the ratio of the two displacements as a function of the time interval Δt.

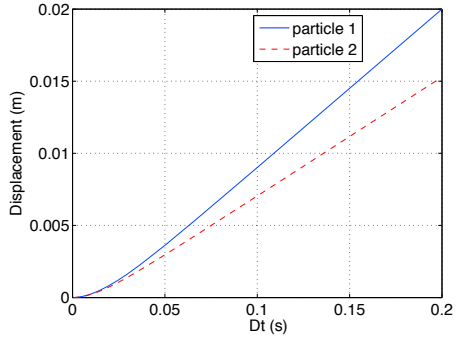

Figure 3. Step length x_1, x_2 vs pulse width Δt.

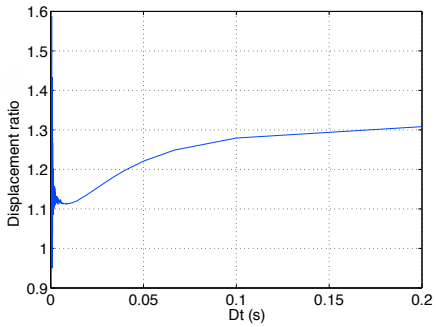

Figure 4. Ratio of step lengths vs pulse width Δt.

As long as the pulse widths correspond to different displacement ratios, the matrix **R** will have full rank and unique solution for n_1 and n_2 will exist. Since the particles come to rest between pulses, the sequential ordering of the pulses will affect the path, but will not affect the final locations of the particles. Note that, in general, arbitrary desired displacements will not correspond to integer numbers of pulses resulting in small errors in actual displacement. These can be reduced by repeating the procedure using pulses of shorter duration and thus displacement.

IV. Simulation Results

Simulations were performed to demonstrate the efficacy and accuracy of the motion planner and also the effect of the sequential ordering of the pulses. The parameters used in all simulations are listed in Table 1. In subsection A, the particles are constrained to move only along the x-axis. Subsection B presents an optimization scheme that explores the tradeoff between displacement time and error.

TABLE 1. SIMULATION PARAMETERS

Parameter	Value
Radius r_1 of ferrous sphere encapsulated in capsule 1. [m]	0.0005
Radius r_2 of ferrous sphere encapsulated in capsule 2. [m]	0.00075
Radius of capsule 1. [m]	0.0015
Radius of capsule 2. [m]	0.003
Density of ferrous spheres ρ_1, ρ_2 [Kg/m^3]	7850
Density of capsule shell (resin) [Kg/m^3]	1174
Density of the fluid [Kg/m^3]	1000
Dynamic viscosity of the fluid [Pas]	1.0 10^{-3}
Magnetization of ferrous spheres [Am^{-1}]	1.36 10^6
Magnetic gradient amplitude [T/m]	0.02

A. 1-D simulation along the x-axis

The following three simulations demonstrate that the algorithm is able to generate motion plans that independently drive the particles to their goals. Their initial positions are set to $x_{1i} = x_{2i} = 0mm$.

Simulation 1: In this example, the position of particle 1 is kept fixed while particle 2 is programmed to move 10mm along the positive x-axis, i.e. the goal is set to $x_{1f} = 0mm,\ x_{2f} = 10mm$.

A plot of the step length versus the pulse width (similar to that of Figure 4) is generated by the algorithm and is used to select appropriate pulse widths. The selected pulse widths are Δt_1=0.1s, Δt_2=0.037s. These widths were selected because the two points are sufficiently apart to ensure that the response matrix is not singular and at the same time result in pulses of reasonable width (not extremely short or large). Also they were selected because, as it will be shown shortly, their ratio n_2 / n_1 is approximately an integer value. The corresponding step lengths are given in Table 2:

TABLE 2. MOTION PLANNING PARAMETERS

	$\Delta t_1 = 0.1$s	$\Delta t_2 = 0.037$s
Step length x_1 (m)	0.01064	0.005394
Step length x_2 (m)	0.007815	0.004147

The control matrix **R** is given by:

$$\mathbf{R} = \begin{bmatrix} x_1(\Delta t_1) & x_1(\Delta t_2) \\ x_2(\Delta t_1) & x_2(\Delta t_2) \end{bmatrix} = \begin{bmatrix} 0.01064 & 0.005394 \\ 0.007815 & 0.004147 \end{bmatrix} \quad (7)$$

The n_1 and n_2 are found using Eq. (6). Their values are given by $n_1 = -27.4,\ n_2 = 54$. For implementation, these numbers are rounded to integer values, $n_1 = -27,\ n_2 = 54$, and a negative sign indicates pulses of negative amplitude. The constructed pulse sequence comprises a repetition of a Δt_1 pulse followed by n_2 / n_1 pulses of Δt_2 (in this case $n_2 / n_1 = 2$). All n_1 and n_2 pulses were interleaved by equal number of Δt_{off} zero amplitude pulses.

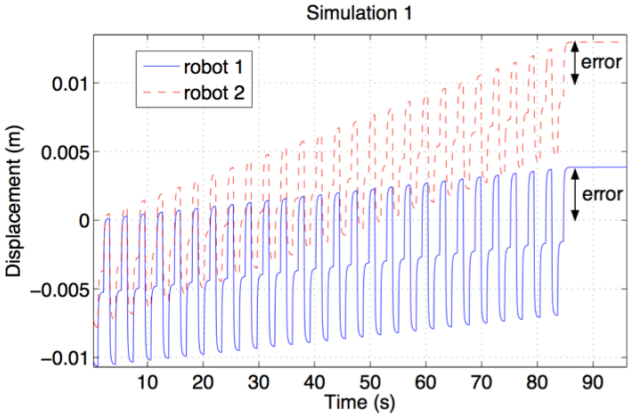

Figure 5. Simulation 1. Desired displacements of robot 1 and robot 2 are 0 and 10 mm, respectively.

In the plot of Figure 5, the response due to the pulse sequence is clearly depicted: a longer response due to $\Delta t_1 + \Delta t_{off}$ followed by two consecutive $\Delta t_2 + \Delta t_{off}$ pulses. The final error for each particle position is less than half its Δt_1 response and is due to the rounding of the value of n_1 (the remainder of the rounding is 0.4 of the Δt_1 response). Furthermore, it is clear that the motion response exhibits an oscillation whose amplitude is approximately equal to the Δt_1 response. Greater accuracy requires selecting smaller Δt values that result in smaller step length and thus in higher motion resolution, of course at the expense of time.

Simulation 2: In this example, the desired particle displacements are interchanged, i.e., $x_{1f} = 10mm,\ x_{2f} = 0mm$. The motion planning algorithm yields $n_1 = 43,\ n_2 = 87$ for $\Delta t_1 = 0.0175s,\ \Delta t_2 = 0.058s$ and the resulting motions are depicted in Figure 6. In this example, the final position error is only 10% of the goal value. The decrease of the error is due to the very small size of the pulse widths $\Delta t_1, \Delta t_2$ (and the corresponding responses). Note however that it takes more time to reach the goal.

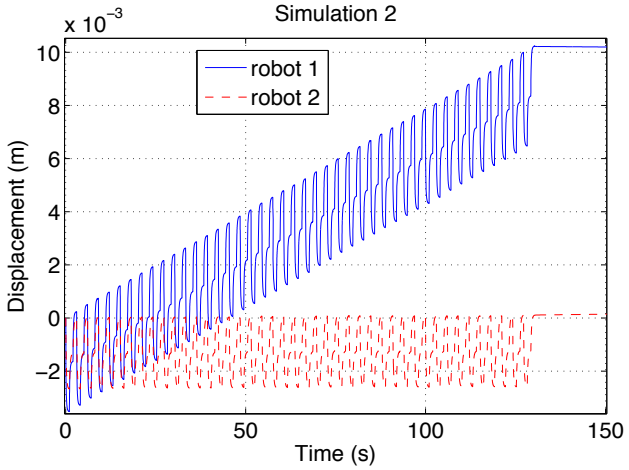

Figure 6. Simulation 2. Desired displacements of robot 1 and robot 2 are 10 and 0 mm, respectively.

Simulation 3: The first simulation example is now repeated but with a different sequential order of pulses to demonstrate how the sequential order affects the path of the

particles. Here, all 27 negative Δt_1 pulses are performed first followed by the 54 positive Δt_2 pulses. While this results in the same final error for both particles, failure to interleave the positive and negative amplitude pulses results in large overshoot for both particles.

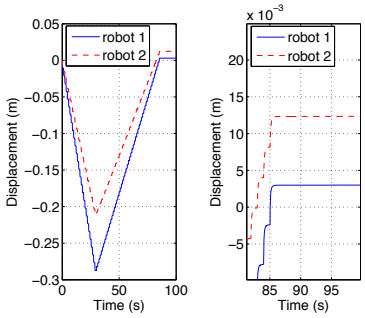

Figure 7. Simulation 3. Desired displacements are the same as Simulation 1, but the order of pulses is changed.

B. *Optimizing the selection of Δt_1, Δt_2 pulse widths*

Simulations 1 and 2 demonstrate how the choice of pulse widths can affect both the time required to complete a desired displacement as well as the final position error due to pulse number rounding. To investigate this tradeoff, this subsection defines an objective function incorporating these two variables.

For a desired set of displacements, (x_1^f, x_2^f), the total time is given by

$$t_{total} = |n_1|\Delta t_1 + |n_2|\Delta t_2 + (|n_1| + |n_2|)\Delta t_{off} \quad (8a)$$

$$n_1 = \frac{(x_2(\Delta t_2)x_1^f - x_1(\Delta t_2)x_2^f)}{(x_1(\Delta t_1)x_2(\Delta t_2) - x_2(\Delta t_1)x_1(\Delta t_2))} \quad (8b)$$

$$n_2 = \frac{(-x_2(\Delta t_1)x_1^f - x_1(\Delta t_1)x_2^f)}{(x_1(\Delta t_1)x_2(\Delta t_2) - x_2(\Delta t_1)x_1(\Delta t_2))} \quad (8c)$$

Assuming that the number of pulses applied is obtained by rounding the values provided by the motion planning algorithm, the maximum displacement error for a pulse width pair Δt_1, Δt_2 can be calculated as follows:

$$e_{total} = \sqrt{e_1^2 + e_2^2} \quad (9)$$

$$e_1 = \max\{x_1(\Delta t_1)/2,\ x_1(\Delta t_2)/2\} \quad (10a)$$

$$e_2 = \max\{x_2(\Delta t_1)/2,\ x_2(\Delta t_2)/2\} \quad (10b)$$

The optimal pair $(\Delta t_1^*, \Delta t_2^*)$ is defined as the one that minimizes the objective function given by

$$J = w_1 e_{total}(\Delta t_1, \Delta t_2,) + w_2 t_{total}(\Delta t_1, \Delta t_2,) \quad (11)$$

where w_1, w_2 are weighting coefficients. The following figure depicts the surface of $J(\Delta t_1, \Delta t_2)$ and indicates the pair ($\Delta t_1, \Delta t_2$) that minimizes J . There are two symmetric surfaces corresponding to the pairs $(\Delta t_1^*, \Delta t_2^*)$ and $(\Delta t_2^*, \Delta t_1^*)$.

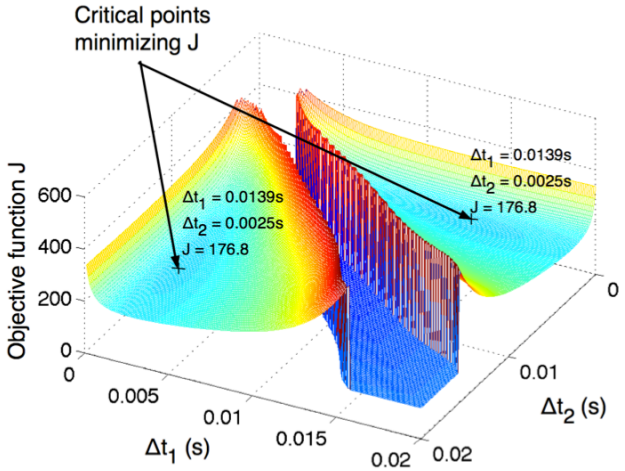

Figure 8. Plot of objective function for $x_1^f = 0mm$, $x_2^f = 10mm$.

V. Motion Planning Experiments

To test the motion planning algorithm in an MRI scanner, hollow spherical capsules were fabricated as hemispheres using a 3D printer (Objet, Inc.). The larger capsule had an external diameter of 5mm and a wall thickness of 1mm. The smaller capsule had an external diameter of 3mm and a wall thickness of 0.7mm. Chrome steel spheres were placed inside each cavity of the hemispheres which then were glued together (Figure 9).

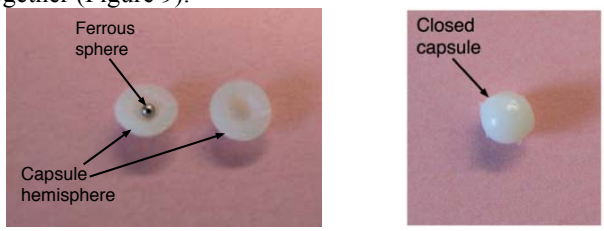

Figure 9. Capsule: (a) Capsule shell and ferrous sphere, (b) Closed capsule.

The magnetization of the chrome steel becomes saturated as soon as it is introduced into a magnetic field greater than 2T. Its saturation magnetization value is M_s = 1.6 10^6 Am^{-1}.

Before insertion into the MRI bore, the capsules were placed inside two plastic tanks half-filled with water (Figure 10). They were then stacked on top of each other and inserted inside the bore of a 9.4 Tesla (BioSpec 94/20,Biospin) research MRI scanner that employs a 400 mT/m gradient coil with inner diameter, 120 mm. The upper tank contained the small capsule, while the lower tank contained the larger capsule (Figure 10). The stacked tanks are required to keep the magnetized capsules at sufficient distance apart to minimize magnetic interaction. During the experiments only the *x*-gradient was activated to aid in optical visualization of particle motion. Particle location and motion were recorded by video camera.

The initial position of the particles along the x-axis was randomly generated, and was measured to be x_{1i} = 10mm for the large capsule and x_{2i} = 25mm for the small capsule with respect to the left wall of the tank.

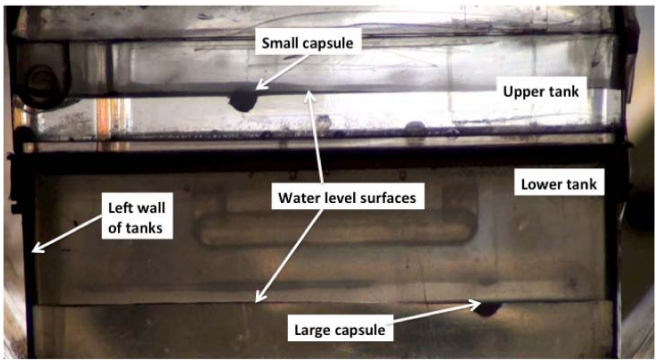

Figure 10. Experimental set up in MRI scanner.

The experimental scenario requires moving the particles one cm closer to the origin, i.e. towards the left wall, at x_{1f} = 0mm and x_{2f} = 1.5mm. The physical parameters of the system were either measured or obtained by data sheets. The parameter values are those already presented in Table 1.

The motion planning algorithm was run and generated a pulse sequence for driving the capsules to the goal. To simplify the implementation of the MRI program we adopted the approach of pulse sequential order shown in simulation 2. Therefore, we first applied $n_1 = \text{int}(22.3)$ pulses of duration $\Delta t_1 = 0.1s$ followed by $n_2 = \text{int}(57.5)$ pulses of duration $\Delta t_1 = 0.0397s$. The experimental results are superimposed on the simulation results in Figure 11. Future implementations will adopt the approach presented in simulations 1 and 2 to minimize the overshoot of the path followed by the particles.

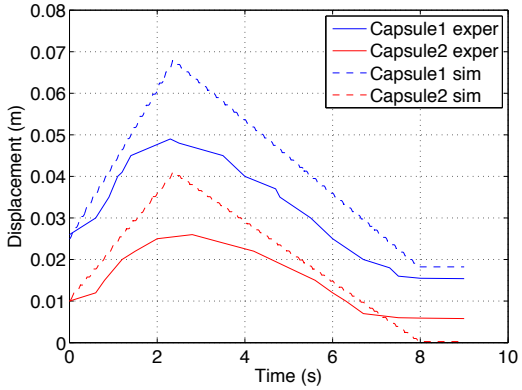

Figure 11. Comparison of experimental and simulation results of the capsules trajectories.

The expected theoretical error is in the range 2-3mm based on the amplitude of the step responses for the given pulse widths. The actual error twice as that.

There is also a discrepancy of 2.5 cm in the overshoot of the experimental and simulated trajectories. The sources of this discrepancy are the inaccuracies in the estimated values of physical parameters, the assumption that the two particles do not interact magnetically, the non-linearity of the magnetic gradients towards the boundaries of the bore and also the surface tension forces imparted by the walls to the capsules.

VI. Conclusion

Magnetically powered tetherless robots hold great promise for medical applications. Since many interesting applications involve controlling groups of robots, it is important to analyze the controllability of such systems and to develop motion planning strategies. This paper presents the first results of this type for millimeter-scale swimming robots. The proposed motion planning algorithm exploits inertial transients together with the nonlinear damping to produce differentiated motion. Experimental results corroborate the theory. Future work will develop more accurate dynamic models and consider larger numbers of robotic capsules.

References

[1] J.-B. Mathieu, and S. Martel, 2007. “Magnetic microparticle steering within the constraints of an MRI system: proof of concept of a novel targeting approach”, Biomedical Microdevices 9, 801-808.

[2] B. Behkam, and M. Sitti, 2007. "Bacterial flagella-based propulsion and on/off motion control of microscale objects," Ap. Ph. Letters 90 (2), 1-3.

[3] K. B. Yeşin, K. Vollmers, B. J. Nelson, "Modeling and control of Untethered Biomicrorobots in a Fluidic environment using Electromagnetic Fields", International Journal of Robotics Research, Vol. 25, No. 5-6, 2006, 527--536.

[4] L. Arcese, M. Fruchard and A. Ferreira, "Nonlinear modeling and robust controller-observer for magnetic microrobot in a fluidic environment using MRI gradients," Proceedings IEEE Int. Conference on Intelligent Robotics and Systems, St. Louis, USA, 2009.

[5] G. Kosa, P. Jakab, N. Hata, F. Jolesz, Z. Neubach, M. Shoham, M. Zaaroor, G. Szekely, “ Flagellar swimming for medical micro robots: Theory, experiments and application”, Biomedical Robotics and Biomechatronics, 2008. BioRob 2008. 2nd IEEE RAS & EMBS International Conference on.

[6] C. Bergeles, M. P. Kummer, B. E. Kratochvil, C. Framme and B. J. Nelson, “Steerable intravitreal inserts for drug delivery: In vitro and ex vivo mobility experiments”.

[7] P. Pouponneau, J.-C. Leroux, S. Martel, "Magnetic nanoparticles encapsulated into biodegradable microparticules steered with an upgraded magnetic resonance imaging system for tumor chemo-embolization”, Biomaterial 30 (2009), pp. 6327-6332.

[8] E. Diller, S. Floyd, M. Sitti, "Control of multiple heterogeneous magnetic micro-robots in non specialized surfaces", IEEE International Conference on Robotics and Automation (ICRA), 2011, 9-13 May 2011, Shanghai, China.

[9] Z. Zhang, Y. Huang, Chia-Hsiang Menq, “Actively Controlled Manipulation of a Magnetic Microbead Using Quadrupole Magnetic Tweezers”, IEEE Transactions on Robotics, 26 Issue: 3, June 10.

[10] F, O. Aboussouan, E. Chanu, A. Martel, S., “Real-time positioning and tracking technique for endovascular untethered microrobots propelled by MRI gradients”, IEEE International Conference on Robotics and Automation, 2009. ICRA '09.

[11] F. M. White, Fluid Mechanics, 5th ed., McGraw-Hill Science, 2003.

[12] J. J. Abbott, O. Ergeneman, M. Kummer, A. M. Hirt, B. J. Nelson, "Modeling Magnetic Torque and Force for Controlled Manipulation of Soft-Magnetic Bodies", IEEE Transactions on Robotics, Vol. 23, No. 6, December 2007, pp. 1247--1252.

[13] P. Vartholomeos, L. Qin and P. Dupont, “MRI-powered Actuators for Robotic Interventions”, IEEE International Conference of Intelligent Robots and Systems (IROS 11), San Francisco, CA, September 2011.

[14] P. Vartholomeos, C. Mavroidis, "Simulation Platform for Self-assembly Structures in MRI-based Nanorobotic Drug Delivery System", IEEE International Conference on Robotics and Automation (ICRA 10), 3-8 May 2010, Anchorage, Alaska, USA.

[15] H. J. Sussmann. “A general theorem on local controllability”, SIAM Journal on Control and Optimization, 25(1):158-194, Jan 1987.